Modeling and Design of GeSn Avalanche Photodiodes With High Tin Content for Applications at 3.3 μm

Lorenzo Finazzi, Raffaele Giani, Omar Concepción, Dan Buca, Vincent Reboud, Giovanni Isella, and Alberto Tosi, *Member, IEEE*

***Abstract*—We propose and compare two back-side illuminated GeSn avalanche photodiode (APD) mesa structures with 15% tin content operating at photon wavelengths up to 3.3 μm, suitable for applications like methane gas sensing and analysis of tampered olive oil. The two structures have different multiplication materials: a) silicon, which requires an additional Ge Strain-Relaxed Buffer (SRB) layer for high-quality GeSn growth; b) germanium, which is acting also as SRB layer. The latter design is innovative compared to the state-of-the-art and it proposed to: i) reduce the space charge region (SCR) width by avoiding a too thick Ge SRB, which is required for growing high-tin-content GeSn; ii) avoid one supplementary non-lattice matched heterojunction in the SCR. Physical models for GeSn are discussed for the most relevant parameters of APD design. Simulations are performed in the electrical and optical domains, for evaluating the main figures of merit of APDs and comparing the expected performances between the two designs. Finally, we present the modeling and design of a focalizing all-dielectric metalens, integrated on the detector back-side, for improving the photon collection efficiency at the same active volume size, thus improving the signal-to-noise ratio.**

***Index Terms*—Avalanche PhotoDiode (APD), germanium tin, medium infra-red radiation (MIR), metalens integration, MIR sensing application.**

I. Introduction

MEDIUM Infra-red (MIR) radiation (between 3 and 50 μm) is widely exploited for various applications. In detail, 3.3 μm radiation is also exploited for methane gas detection [1] and for the analysis of tampered olive oil [2], as investigated within the Horizon Europe project "LastStep".

Currently-available MIR detectors can be divided into two families: bolometers and photodetectors [3]. The former ones are based on the detection of temperature variation due to radiation absorption, but they are affected by ambient temperature fluctuations and their response time is slow. The latter ones exploit the electron-hole pair photogeneration in different semiconductors, such as HgCdTe, HgZnTe, InSb and InAs. More complex solutions are based on GaAs/AlGaAs quantum well superlattices and InAs/GaInSb strained layer superlattices [3], which contain expensive and rare elements.

Germanium-Tin ($Ge_{1-x}Sn_x$) is a group IV alloy that is much more affordable compared to the previously-mentioned compounds and its fabrication is considered CMOS compatible, enabling the design of cost-effective photodetectors for different spectral regions, from the SWIR (Short Wave InfraRed) to part of the MIR regions, as its bandgap can be tuned by selecting the tin content [4]. Additionally, GeSn LASER [5], [6], [7] and LED [8], [9] sources have been demonstrated, thus opening the path towards the demonstration of a group IV active photonic circuits [10].

Few linear-mode APDs based on GeSn are reported in literature [11], [12], [13], all with low tin content (up to 10%), showing cut-off wavelength far below 3.3 μm. When the tin percentage rises, the SRB layer has to be thicker for growing high quality GeSn [4] and the non-intentional doping (NID) level becomes non negligible, giving issues mostly in the avalanche multiplication layer, where the electric field has to be ideally high and constant. Additionally, the built-in compressive stress of the GeSn grown on Ge shifts the cut-off wavelength of GeSn toward shorter wavelengths. Increasing Sn content extends the cut-off, but also enhances compressive strain.

In this paper, we discuss the above-mentioned problems and propose two structures for high Sn content GeSn-based linear-mode APDs. In Section II, physical models of the most relevant GeSn parameters for modeling purposes are discussed. In Section III, two designs for GeSn-based APDs with 15% Sn content, suitable for methane gas detection and tampered olive oil analysis, are presented. Simulations are performed for extracting the most relevant figures of merit. The performances of the two designs are then discussed, identifying the best

Manuscript received 31 May 2024; revised 31 July 2024; accepted 2 August 2024. Date of publication 6 August 2024; date of current version 3 September 2024. This work was supported by European Union's Horizon Europe Research and Innovation Program under Grant 101070208. *(Corresponding author: Lorenzo Finazzi.)*

Lorenzo Finazzi and Alberto Tosi are with the Dipartimento di Elettronica, Informazione e Bioingegneria, Politecnico di Milano, 20133 Milano, Italy (e-mail: lorenzo.finazzi@polimi.it; alberto.tosi@polimi.it).

Raffaele Giani and Giovanni Isella are with the Dipartimento di Fisica, Politecnico di Milano, 20133 Milano, Italy (e-mail: raffaele.giani@polimi.it; giovanni.isella@polimi.it).

Omar Concepción and Dan Buca are with the Peter-Grünberg-Institute (PGI-9) and JARA-Fundamentals of Future Information Technologies, Forschungszentrum Jülich 52428, Germany (e-mail: o.diaz@fz-juelich.de; d.m.buca@fz-juelich.de).

Vincent Reboud is with the CEA Leti, Grenoble 38000, France (e-mail: vincent.reboud@cea.fr).

Color versions of one or more figures in this article are available at https://doi.org/10.1109/JSTQE.2024.3439495.

Digital Object Identifier 10.1109/JSTQE.2024.3439495

© 2024 The Authors. This work is licensed under a Creative Commons Attribution-NonCommercial-NoDerivatives 4.0 License. For more information, see https://creativecommons.org/licenses/by-nc-nd/4.0/

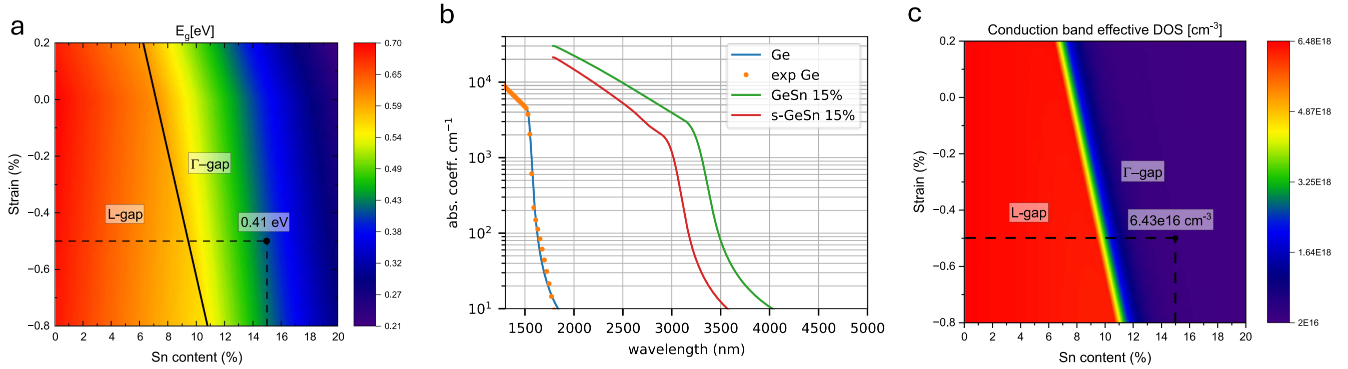

Fig. 1. Bandgap of GeSn as a function of Sn content and residual strain. The plot is divided into direct and indirect transition regions (a). The theoretical and experimental absorption coefficients of Ge are compared to $Ge_{0.85}Sn_{15}$ one, with and without the effect of residual strain $\varepsilon_{\parallel} = -0.5\%$ (b). Conduction band effective density of state showing great decrease across indirect to direct transition (c). All parameters are reported at 200 K.

approach. In Section IV, we propose possible future developments to break the noise *vs.* detection efficiency tradeoff, by exploiting an all-dielectric, CMOS compatible metalens optimized for 3.3 μm radiation.

II. Physical Models

In this paragraph, we will discuss models of GeSn physical parameters relevant for simulations, including their dependence on Sn content, temperature and strain on the band structure, and optical absorption. Material degradation due to lattice mismatch and low temperature epitaxy is discussed.

A. Germanium-Tin Alloy

The band-structure of $Ge_{1-x}Sn_x$ alloy is strongly affected by Sn content and residual strain. For a Sn content x $\approx$ 8%, relaxed $Ge_{1-x}Sn_x$ becomes a direct-gap semiconductor with the conduction band minimum at the Γ-point of the Brillouin zone.

In $Ge_{1-x}Sn_x$/Ge heteroepitaxial layers, residual compressive strain due to the partial relaxation of strain pushes the indirect-to-direct transition to larger Sn contents [9].

Fig. 1(a) shows the evolution of the energy gap E_g for different Sn contents and strain levels at T = 200 K. The relevant physical parameters required for the calculation of E_g (temperature dependent bandgaps of Ge and α-Sn, bowing parameters and deformation potentials) were taken from [14]. Device modelling reported in the next sections was performed assuming x = 15% and a residual compressive strain $\varepsilon_{\parallel} = -0.5\%$ (a typical value for GeSn epilayers) resulting in $E_g = 0.41$ eV with a Γ-L energy separation of $\sim$ 0.1 eV.

Direct-gap $Ge_{1-x}Sn_x$ alloys feature a strong absorption coefficient in the mid-IR [15]. The absorption coefficient was calculated using the model reported in [16] and originally developed for Ge. Fig. 1(b) shows the calculated absorption coefficient for Ge (compared with experimental data taken from [17]) and that of relaxed and strained $Ge_{0.85}Sn_{0.15}$ alloys. Due to the lack of reliable data on the refractive index n for $Ge_{1-x}Sn_x$ alloys with x > 12% [15], n was extracted from $n^2 = \kappa^2 + \varepsilon_1$, where ε_1 is the real part of the dielectric function of Ge and κ the extinction coefficient of $Ge_{0.85}Sn_{0.15}$ obtained from the calculated absorption coefficient.

Since the effective mass of Γ valley electrons is approximately an order of magnitude smaller than that of L valleys electrons, the indirect-to-direct transition is accompanied by a strong reduction of the conduction band density of states (see Fig. 1(c)). This effect should partially mitigate the increase in intrinsic carrier density and, as a consequence, in dark current, expected at large Sn concentrations. However, the low deposition temperature, required to avoid Sn segregation and plastic relaxation, introduces vacancies and dislocations in the epilayer. Such defects feature an acceptor-like character leading to a p-type non-intentional doping (NID) of approximately $9 \cdot 10^{17}$ cm^{-3}, as reported in [18], giving a strong gradient of the electric field that reduces the space charge region (SCR) width. As a result, many photons are absorbed outside the SCR and the photogenerated carriers are collected only after their diffusion towards the SCR. Given such transport mechanism, GeSn thickness has to be about one diffusion length beyond the SCR. A too thick GeSn absorption layer would just degrade the noise without any advantage in the photon detection. The diffusion length L_{diff} is:

$$L_{diff} = \sqrt{D \cdot \tau_{diff}} \tag{1}$$

where D is the diffusion coefficient and τ_{diff} is the minority carrier lifetime. The values of these parameters have been estimated from the few data available in literature. We used D_e = 12.31 cm^2/s and D_h = 24.62 cm^2/s for diffusion coefficients for electrons and holes, as reported in [19] for $Ge_{0.95}Sn_{0.05}$ at 200 K, while no values are reported for higher tin concentration. However, the diffusion coefficient is expected to increase with tin concentration. Minority carrier lifetimes were retrieved from [18] for $Ge_{0.875}Sn_{0.125}$ at 300 K, reporting a value of 130 ps. Despite the operating temperature for the proposed devices is 200 K, lifetime shows low dependency on temperature [18] and the value at 300 K can well represent the one at 200 K.

B. Recombination at Heterointerfaces

Multiplication-based photodiodes are very sensitive to material quality. In particular, lattice mismatched heterojunctions give rise to defects generated from stress accumulation. In the two APD structures presented in this paper, schematically shown in Fig. 2, Ge/Si and GeSn/Ge heterojunctions are present, and their positions influence the overall performance.

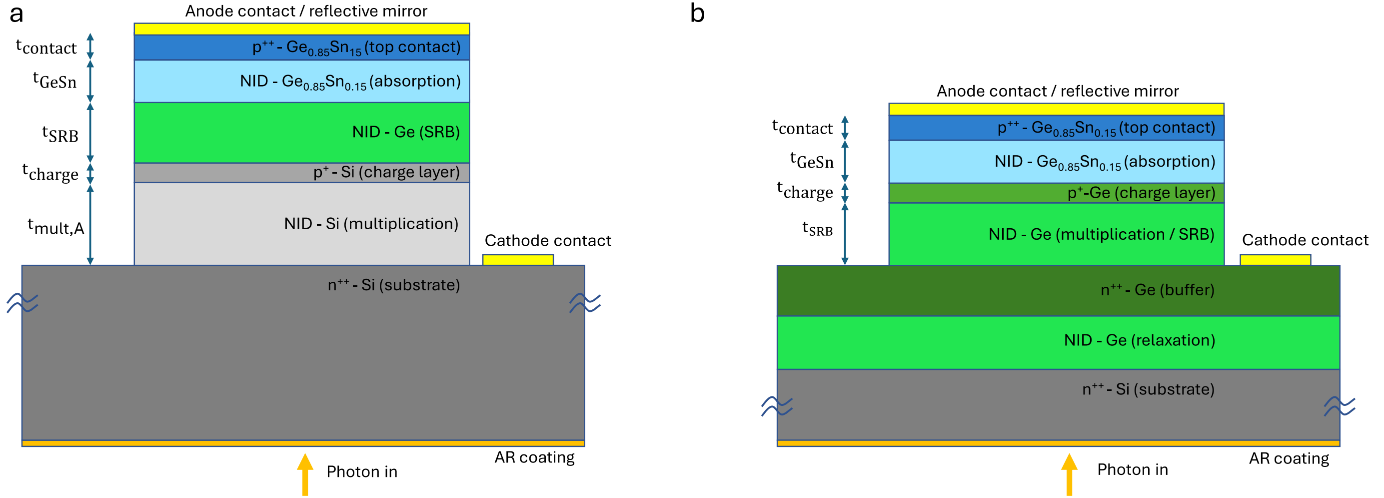

Fig. 2. Schematic cross-section of Design A, where avalanche multiplication is in silicon (a). Schematic cross-section of Design B, where avalanche multiplication is in germanium (b).

Germanium features a lattice mismatch of about 4.2% with respect to silicon. This non-negligible difference generates plastic deformation, resulting in dislocations that act as strong Shockley–Read–Hall recombination centres for minority carriers, enhancing the noise generation. This effect can be included in the simulations by tuning the lifetime of germanium. The recombination rate induced by threading dislocations through the Ge layer can be estimated from the lifetime given by the following equation [20]:

$$\tau_{dislocation} = \frac{0.7}{N_s} \tag{2}$$

for p-type germanium at room temperature, where N_s is the area density of dislocations. The dislocation density is expected to decrease with the inverse square of the distance from the heterointerface, going from a few 10^{10} cm^{-2} within the first $\sim$ 50 nm to a few 10^{6} cm^{-2} when the distance from the interface reaches $\sim$10 μm, as reported in [21]. For simulation purposes, the germanium region was divided into steps, each associated to the corresponding discretized dislocation density and lifetime from (2).

$Ge_{0.85}Sn_{0.15}$ also features a lattice mismatch with Ge of $\sim$ 2.2%. When GeSn-based devices need to be integrated on silicon photonic platform, the growth of high quality, high tin content GeSn is facilitated by a thick germanium SRB layer between Si and GeSn [22]. Differently from Ge/Si interface, to the best of our knowledge, in literature no relation between minority carrier lifetimes in GeSn and mismatch-related defects is available. For this reason, the recombination-generation in the GeSn layer was modelled by using a uniform lifetime of 130 ps, as reported in [18] (note that the lifetime of GeSn might vary from tens of picoseconds to a few nanoseconds depending on Sn concentration and temperature). It must be noted that the GeSn/Ge hetero-interface is present in both GeSn APD designs and we expect it to play a minor role when considering a relative comparison between *Design A* and *B*. To validate this argument, we also performed simulations setting the lifetime of GeSn one decade lower (i.e., 13 ps) with respect to the literature one. This is done to increment the contribution to overall noise and signal loss from Ge/GeSn hetero-junction and analyze also in a worst case scenario the relative performances of the two designs under investigation. Despite the GeSn's lifetime was reduce by one order of magnitude, the noise associated to Ge/Si interface was still dominant, confirming GeSn/Ge interface has minor impact on overall generation.

III. GeSn-Based APD Designs

APDs working principle is based on the possibility to multiply photogenerated carriers by means of impact ionization [23]. This translates into higher sensitivity, gain and bandwidth compared to p-i-n photodiodes. However, also carriers generated in dark conditions are multiplied. In this section, we present two APD designs with $Ge_{0.85}Sn_{0.15}$ absorption layer (Fig. 2). The devices are engineered to be manufactured on silicon wafers, for their compatibility with CMOS silicon photonic platforms. Both structures are based on SACM (Separate Absorption Charge Multiplication) designs, already proven to be effective for APD detectors. Back-illumination is used to enhance the absorption of incoming photons by exploiting a double pass through the absorption region and filter out short-wavelength radiation.

The multiplication material in *Design A* is silicon, while it is germanium in *Design B*. The thickness of the Ge SRB layer is chosen to be $t_{SRB} = 1.5$ μm, while that of the charge layer is $t_{charge} = 20$ nm, for both structures. The diffusion length of electrons (which initiate the avalanche multiplication) is $L_e =$ 565 nm, so that the optimal thickness of GeSn layer is about $t_{GeSn} = L_e$.

The radius of the active area was set to 5 μm, small enough for short simulation times. Finally, a SiO_2 antireflection coating (with λ/4 thickness) is considered on the back of the structures and a p^{++} GeSn layer (thickness $t_{contact} = 50$ nm) is used to

guarantee ohmic contact on the anode side. All the simulations are performed at a temperature of 200 K, which can be achieved by means of a simple multi-stage thermo-electric cooler.

A. Design A

As shown in Fig. 2(a), the stack of the first structure resembles the one discussed in [11]. However, GeSn for 3.3 μm radiation needs a much higher tin content of around 15% (with respect to the 5%-10% used in [11] and [12]), thus requiring a thick Ge SRB layer before GeSn growth and also leading to a high non-intentional doping level in the absorbing material. Its main advantage is that avalanche multiplication is electron-initiated in silicon, whose low k (i.e., the ratio between holes and electrons ionization coefficients) leads to a low excess noise factor [24]. The thickness of the silicon multiplication region is set to $\mathrm{t_{mult,A,}}$ $= 1.5$ μm. Such thickness is chosen to be equal to that of the SRB/multiplication layer of *Design B*.

The dark current is proportional to the active volume of the device, thus making the Ge SRB layer contributing to this unwanted phenomenon. Passivation of Si sidewalls is a well-established technique [25], which allows to safely neglect generation from sidewall surface for Design A. Recently, strategies involving oxidation and nitride deposition have been reported for Ge passivation [26], [27], leading to interface state densities similar to those typically reported for Si. Therefore, also in the case of Design B the role of lateral surface generation has been neglected. Overall, the Ge SRB layer does not directly contribute to any optical and electrical parameter of the APD, since it is present just for improving the quality of the GeSn layer, but it contributes to the noise. Additionally, such Ge SRB layer increases the APD breakdown voltage, which is not convenient in practical applications.

Another issue of *Design A* is associated to the presence inside the active volume of two non-lattice matched heterojunctions, i.e., GeSn/Ge and Ge/Si. As discussed in Section II, the dislocations resulting from such hetero-interfaces strongly contribute to the dark current. In the following *Design B*, one of such hetero-interfaces is kept outside the active volume, thus avoiding its contribution to the dark current.

B. Design B

The second design is novel compared to what reported in literature [11] and it is presented in Fig. 2(b). In *Design B*, the multiplication layer is made of germanium and the SRB layer itself is exploited for this purpose, thus reducing the overall volume of the active region. The thickness of the Ge multiplication layer is $t_{mult,B} = t_{SRB} = 1.5$ μm, like the one of *Design A*, but it can also be increased (or decreased), if needed, for a different trade-off between the different APD parameters. Moreover, in *Design B*, the Ge SRB layer is not grown on silicon, but on relaxed germanium, which leads to higher quality SRB and, eventually, to a GeSn layer with a better crystal-quality. Since non-intentionally doped GeSn shows a high p-type doping, GeSn must be employed on the anode side, as in *Design A*, resulting in electron-initiated avalanche multiplication in the germanium multiplication region. However, differently from silicon, the electron impact ionization coefficient is lower with respect to the hole one in germanium, thus degrading the APD gain. This also translates into higher k value, thus leading to a stronger excess noise factor *F* for electron-initiated avalanche.

In *Design B*, the Ge/Si interface is buried below the active volume, i.e., outside the SCR. A thick NID Ge relaxation layer is grown over the silicon wafer to screen the high defects density region resulting from the non-lattice matched heterojunction. For simplicity purposes, the thickness of both relaxation and buffer Ge layer (see Fig. 2(b)) is set at 1.5 μm. Despite such layers, a few threading dislocations can still be present inside the active volume. On top of the Ge relaxation layer, a highly n-type doped Ge buffer is deposited to serve as cathode contact. Differently from *Design* A, this approach reduces the number of non-lattice matched heterojunctions inside the active volume, just the GeSn/Ge one, thus enhancing the material quality for improving the APD performance.

C. Comparison

Optical and electrical simulations were performed with a commercial Technology Computer Aided Design (TCAD) tool (Synopsys Sentaurus), extracting dark and illuminated current-voltage curves. Then, custom codes (in MATLAB environment) have been written to calculate responsivity *R*, multiplication factor *M*, excess noise factor *F,* noise equivalent power *NEP* and shot noise i_{shot}:

$$R\left[{}^{A}\!/\!{}_{W}\right] = \frac{I_{ph}}{P_{in}} \tag{3}$$

$$M = \frac{I_{e,out}}{I_{e,\ in}} \tag{4}$$

$$F = kM + (1-k)\left(2 - \frac{1}{M}\right), k = \frac{\beta}{\alpha} \tag{5}$$

$$NEP\ [W] = \frac{I_{dark}}{R_{bias}} \tag{6}$$

$$i_{shot}\,[A] = \sqrt{2{*}q{*}I_{ph}{*}F{*}M^2{*}\,(1\ Hz)} \tag{7}$$

where I_{ph} and I_{dark} are the photocurrent and the dark current, respectively; P_{in} is the optical power impinging onto the active area; $I_{e,\ in}$ and $I_{e,\ out}$ are the current of photogenerated electrons that are injected into the SCR from the GeSn layer and electron current exiting the SCR, respectively. R_{bias} is the responsivity calculated at 90% of the breakdown voltage for 3.3 μm radiation. The coefficients α and β represent the electron and hole impact ionization coefficients, respectively. The dependence of impact ionization coefficients on the electric field follows [28] and [29], respectively for germanium and silicon. The overall value of *k* corresponds to the average of β/α values calculated point-by-point over the multiplication region, thus considering the dependence of impact ionization coefficients on the electric field. For the shot noise, we considered a bandwidth of 1 Hz. Additionally, since dark current is very small compared to photocurrent in typical operating conditions, it can be neglected in the calculation of the shot noise itself.

TABLE I
CALCULATED FIGURES OF MERIT OF DESIGN A AND DESIGN B FOR DIFFERENT VALUES OF P-TYPE DOPING DENSITY OF THE CHARGE LAYER AT 0.9 $V_{breakdown}$

	R [A/W]	M	F	NEP/NEP$_{best}$	I$_{shot}$/I$_{shot, best}$
Design A					
$p_{charge} = 0.5\cdot10^{17}$ cm^{-3}	0.031	4.34	1.79	868	1
$p_{charge} = 1.5\cdot10^{17}$ cm^{-3}	0.033	5.06	1.85	584	1.22
$p_{charge} = 3.5\cdot10^{17}$ cm^{-3}	0.055	8.09	2.09	320	2.66
$p_{charge} = 5\cdot10^{17}$ cm^{-3}	0.085	11.1	2.32	294	4.78
$p_{charge} = 7.5\cdot10^{17}$ cm^{-3}	0.005	-	-	5070	-
Design B					
$p_{charge} = 0.5\cdot10^{17}$ cm^{-3}	0.037	7.56	11.7	559	5.94
$p_{charge} = 1.5\cdot10^{17}$ cm^{-3}	0.038	6.90	10.5	38.7	4.35
$p_{charge} = 3.5\cdot10^{17}$ cm^{-3}	0.038	3.87	5.39	1.39	1.71
$p_{charge} = 5\cdot10^{17}$ cm^{-3}	0.038	3.68	5.05	1	1.57
$p_{charge} = 7.5\cdot10^{17}$ cm^{-3}	0.026	4.55	6.50	1.28	1.83

Simulated values for the proposed figures of merit (calculated at a bias voltage of 90% of the breakdown voltage) are summarized in Table I, for different values of charge p-type doping, for both *Design A* and *Design B*. As previously mentioned, the GeSn/Ge hetero-interface was not explicitly modelled and an average recombination time was used to take in to account recombination-generation in the GeSn layer. However, this approach affects the absolute value of the simulated dark current. Since we are mainly focused on the relative comparison between design A and B, the NEP is reported as the ratio between a specific NEP and the best NEP among all investigated structures. With high enough illumination, multiplication factor, responsivity and excess noise factor should not be affected by the uncertainty on dark current and are thus reported as absolute values. However, shot noise depends on the active area size, so we reported its ratio with respect to the best case.

For charge doping $p_{\text{charge}} \leq 5\cdot10^{17}$ cm^{-3}, *Design A* features an increase of R and M, along with a reduction of NEP when charge doping density gets higher. This can be explained by the decrease of electric field inside the Ge SRB (reducing tunneling generation), while enhancing the one inside the multiplication layer (increasing multiplication). However, the electric field inside the SRB must be large enough to transport photogenerated carrier towards the multiplication region. Further increase of the charge doping level is indeed not beneficial to device performance, as seen in the case of $p_{\text{charge}} = 7.5\cdot10^{17}$ cm^{-3}: photogenerated carriers cannot transit inside the Ge SRB layer and recombine, cutting down the responsivity. For this reason, M, F and shot noise cannot be defined for this configuration. Finally, the excess noise factor is kept low in all *Design A* variations, thanks to the low k value of the silicon multiplication layer.

Concerning *Design B*, the space charge region can still penetrate the NID GeSn layer despite its quite high doping level. By changing charge layer doping density, we can tune how much electric field is present in the absorption layer, as shown in Fig. 3(a). $Ge_{0.85}Sn_{0.15}$ features a very short lifetime and, combined with its small bandgap energy, it can be a strong source of tunneling generation. This is shown by the sharp decrease of the NEP when increasing the charge layer doping from $p_{\text{charge}} = 0.5\cdot10^{17}$ cm^{-3} to $3.5\cdot10^{17}$ cm^{-3}. Further increment of p_{charge} beyond $3.5\cdot10^{17}$ cm^{-3} has no effect on the electric field penetration into the GeSn absorption region. This could be exploited during fabrication, by slightly exceeding the target doping of the charge layer, a layer where tolerances are always very tight. Finally, the excess noise factor of *Design B* is higher compared to *Design A* because electron-initiated avalanche multiplication in germanium is not as good as the one in silicon.

By comparing the two designs, it is possible to notice the great decrease of NEP in *Design B* compared to *Design A*, which is due to the expected better material quality of the former one. By excluding the Ge/Si interface from the active volume, the dark current is reduced. Concerning responsivity and multiplication, *Design A* can achieve higher value compared to the other structure (see Fig. 3(b)). This can be ascribed to the higher electric field achievable inside the multiplication region in *Design A*, resulting in increased ionization coefficients, as shown in Fig. 3(c).

The overall photon detection performance of the detector can be analysed with the NEP. Comparing the best proposed designs, NEP of *Design A* is 294 times higher with respect to that of *Design B*, thus showing that the latter is better.

As pointed out before, germanium is not the ideal choice for electron-initiated multiplication, but the shot noise values of the photogenerated currents result comparable among the lowest NEP configurations of the two designs.

Finally, another advantage of *Design B* over *Design A* is its lower breakdown voltage, which is advantageous in practical applications where limited power supply voltages can be managed more easily.

IV. METALENS INTEGRATION

In a standard photodetector, higher photon collection efficiency can be achieved by increasing the active area, at the

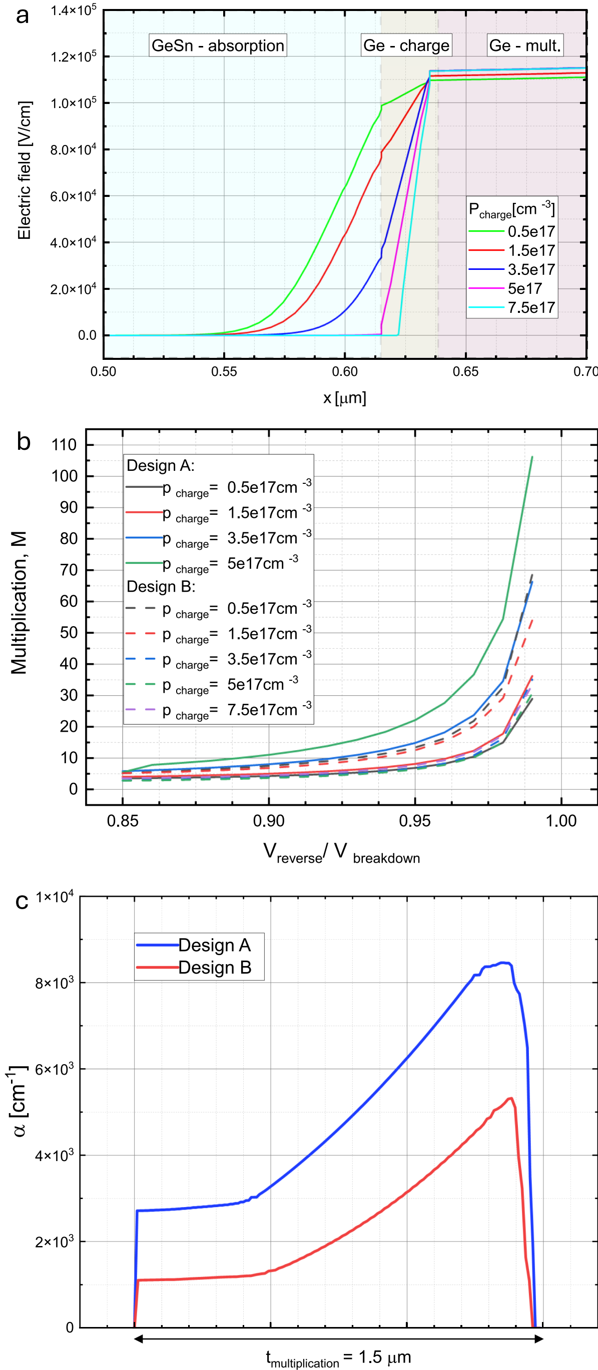

Fig. 3. Electric field profile at GeSn/Ge interface in Design B for different charge layer doping density (a). Multiplication factor of the modelled configurations from 85% to 99% of the corresponding breakdown voltage (b). Electron impact ionization coefficient α in the multiplication region for the best NEP configurations of *Design A* and *Design B* (c).

expense of higher noise (thus degrading the NEP). In order to break such trade-off, focalizing optical elements can increase the photon collection area while keeping the active region small. Microlens have been used for micrometer scale detectors. However, recently-developed metalenses emerged as a valid candidate to substitute refractive lenses [30], [31], because they are less bulky and more flat, thus enabling the possibility to engineer very compact optical systems.

A metalens is an optical element consisting of a periodic composition of nanorods, whose dimensions must be lower than the wavelength of the reference radiation. Exploiting sub-wavelength interaction with the structures, light properties can be manipulated. In addition, compared to classical lenses, metalens have the advantage to possibly manipulate a wider set of radiation properties, including phase and polarization.

We hereby present a polarization-insensitive all-dielectric metalens acting as focalizing element designed for 3.3 μm radiation. The metalens can be monolithically integrated on the back-side of the device and light can be focalized into the active area, also exploiting the metallic mirror on the front-side of the device for a double pass inside the absorbing region. Integration on the back of the device is favourable since a longer focal length is needed with respect to front-side integration, thus enhancing the focalizing efficiency [32]. The proposed metalens is designed in CMOS compatible materials. The substrate is made of silicon dioxide with $\lambda/4$ thickness, while the cylindrical pillars are made of patterned amorphous silicon.

The metalens phase profile is designed to be equivalent to the hyperbolic one:

$$\Phi\left(x,y\right) = -\frac{2\pi}{\lambda_0} n_{sub}\left(\sqrt{x^2+y^2+f^2}-f\right) \tag{8}$$

where x and y are the spatial coordinates on the radiation plane of incidence, λ_0 the vacuum wavelength of the radiation, n_{sub} the refractive index of the device substrate (i.e., silicon), while f is the focal length of the metalens. Without any loss of generality, the radius of the metalens is set at a value of r $=$ 50 μm, while the focal length at f $=$ 350 μm, similar to what we would expect on a real scenario. However, different diameter and focal length can be properly tuned.

The metalens design begins by engineering a single unit cell, composed by a square SiO_2 pedestal (with side length P and height H $=$ 575 nm), on top of which an amorphous silicon cylindrical pillar (with height h and radius r) is grown (Fig. 4(a)). With fixed height, a range of radii must be found so that the unit cell can vary the phase of the incoming radiation over 0-2π range, while preserving the transmission. Then, the complete unit cell database can be exploited to represent every phase shift given by (8). Finite-Difference Time Domain (FDTD) simulations were carried out by a commercial software (Ansys Lumerical) and a valid combination could be found: h $=$ 2.25 μm, P $=$ 1.75 μm and r $\sim$ 250 $\div$ 525 nm. These dimensions yield a maximum pillar aspect ratio of 3.75, making the design feasible with an EBL (Electron Beam Lithography) patterned hard mask plus ICP-RIE (Inductively Couple Plasma - Reactive Ion Etching) fabrication process. The phase and transmission dependence on the radius for the unit cell database are shown in Fig. 4(b). The phase can be modulated over 0-2π range and transmission is kept always above $\sim$85%, apart from radii around 400 nm, which are excluded from the database since they result in poor transmission due to Fabry-Perot like interferences inside the nanorod [33]. The metalens design is built by placing the properly-sized unit cell at a pitch P on a K x K square grid (where K is equal to the ratio between the diameter of the lens and the pitch of the unit cell), yielding the phase shift calculated by (8). The simulated focalizing effect of the metalens for 3.3 μm radiation is shown in

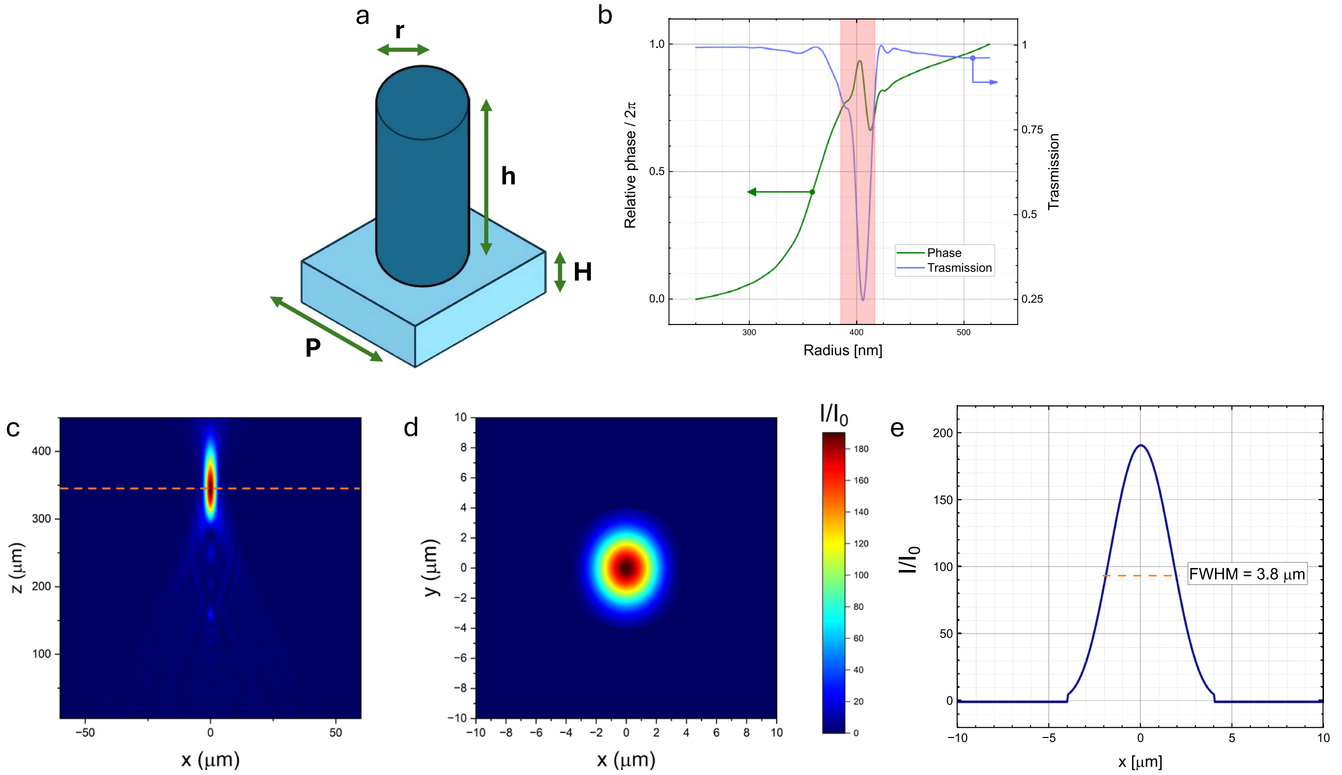

Fig. 4. Illustration of metalens unit cell (a). Relative phase and transmission *vs*. radius of unit cell with fixed height h = 2.25 μm. The region in red is excluded from unit cell database due to low transmission caused by Fabry-Perot interferences inside the nanorod (b). XZ section of simulated relative intensity of focalized radiation after interaction with metalens. The effective focal length is 346 μm (orange dashed line) (c). XY section on the effective focal plane of the relative intensity (d). Cut at x = 0 of relative intensity at effective focal plane. The maximum increase of intensity at focal plane is ~190. The focalized radiation exhibits a FWHM of ~3.8 μm (e).

Fig. 4(c) and (d). The effective focal length is f = 346 μm. The ratio between incoming and transmitted intensity at the focal plane results in a maximum increment of ~190 times and the focal spot features a FWHM of 3.8 μm (Fig. 4(e)). Overall, the design exhibits a $\eta = 30\%$ efficiency, calculated as the ratio between the optical power within four times the FWHM on the focal plane and the impinging power on the metalens [31].

To quantify the advantage of metalens integration, we can compare the photon collection of a device with the same radius of the designed metalens (i.e., 50 μm) and one with 2.5 μm radius, suitable to collect the focalized radiation from the metalens. In particular, the more representative figure of merit for assessing the performance improvement is the NEI (Noise Equivalent Intensity), which is the minimum impinging optical intensity to generate a photocurrent equal to the dark one:

$$NEI = \frac{I_{dark}}{R{*}A_{collection}} \tag{9}$$

where I is the incoming optical intensity, while $A_{collection}$ represents the photons collection area. The dark current I_{dark} scales linearly with the active area of the device (if the peripheral dark current is negligible). A reduction by a factor 400 of dark current occurs when scaling the radius from 50 μm to 2.5 μm. The photocurrent increases linearly with the active area. The 50 μm radius device can thus provide 400 times the photocurrent with respect to the 2.5 μm one, at a given incoming optical intensity I. Also, the responsivity R does not vary with the area, on first approximation.

For the 50 μm device, $A_{collection}$ is equal to the active area while, for the 2.5 μm one with a metalens, the collection area is equal to a device with 50 μm radius as well. However, the non-unitary focusing efficiency η of the metalens must be taken into account. We thus obtain:

$$\frac{NEI^{no-metalens}}{NEI^{metalens}} = \frac{400 * I_{dark,\,0}/R_0 * A_{r\,=\,50\mu m}}{I_{dark,\,0}/R_0 * A_{r\,=\,50\mu m} * \eta} = 120$$

In conclusion, with a simple CMOS-compatible metalens, the minimum optical intensity impinging onto the device that provides a unitary signal-to-noise ratio is reduced by a factor 120. This gives the opportunity to exploit the low dark current from the small active area device combined with the large collection efficiency of a wide metalens.

V. Conclusion

In this article, we presented two APD designs based on $Ge_{0.85}Sn_{0.15}$ absorption layer for methane and tampered olive oil detection. *Design A* exploits silicon as multiplication material, while *Design B* germanium. The former presents a Ge-on-Si heterointerface within the active volume, while in the latter the interface is buried below the space charge region. While the former design was already reported in literature, the latter is a novel and promising approach. TCAD simulations in

electrical and optical domain were carried out to assess dark and illuminated current of the devices. Material degradation due to Ge/Si interface was implemented in the model by tuning the recombination lifetime as a function of dislocations density inside germanium. Considering the configurations with the highest responsivity from the two structures, in *Design A* we could reach approximately twice the responsivity value with respect to *Design B* thanks to the higher electric field in the multiplication region. However, the NEP of *Design A* showed an increment of 294 times with respect to *Design B,* due to the presence of the Ge/Si interface. In addition, despite electron-initiated avalanche multiplication is exploited in germanium, *Design B* showed shot noise comparable to that of *Design A*. Overall, *Design B* features better detection performances at 3.3 μm. Finally, a monolithically integrable CMOS-compatible, all-dielectric metalens can improve the collection capabilities of the device while keeping active area low.

As a perspective, this study on the design of linear-mode APDs might influence the design of future GeSn SPADs (single-photon avalanche diodes), as they both need to minimize the main contributions to carrier generation from the device bulk.

References

[1] B. A. Matveev et al., "Backside illuminated In(Ga)As/InAsSbP DH photodiodes for methane sensing at 3.3 um," *Proc. SPIE*, vol. 4650, pp. 173–178, 2002, doi: 10.1117/12.467661.

[2] A. González-Pereira et al., "State-of-the-art of analytical techniques to determine food fraud in olive oils," *Foods*, vol. 10, no. 3, Mar. 2021, Art. no. 3, doi: 10.3390/foods10030484.

[3] A. Rogalski, "History of infrared detectors," *Opto-Electron. Rev.*, vol. 20, no. 3, pp. 279–308, Sep. 2012, doi: 10.2478/s11772-012-0037-7.

[4] V. Reboud et al., "Advances in GeSn alloys for MIR applications," *Photon. Nanostructures - Fundam. Appl.*, vol. 58, Feb. 2024, Art. no. 101233, doi: 10.1016/j.photonics.2024.101233.

[5] S. Wirths et al., "Lasing in direct-bandgap GeSn alloy grown on Si," *Nature Photon.*, vol. 9, no. 2, pp. 88–92, Feb. 2015, doi: 10.1038/nphoton.2014.321.

[6] J. Chrétien et al., "Room temperature optically pumped GeSn microdisk lasers," *Appl. Phys. Lett.*, vol. 120, no. 5, Feb. 2022, Art. no. 051107, doi: 10.1063/5.0074478.

[7] A. Bjelajac et al., "Up to 300 K lasing with GeSn-on-insulator microdisk resonators," *Opt. Exp.*, vol. 30, no. 3, pp. 3954–3961, 2022, doi: 10.1364/OE.449895.

[8] M. Oehme et al., "GeSn heterojunction LEDs on Si substrates," *IEEE Photon. Technol. Lett.*, vol. 26, no. 2, pp. 187–189, Jan. 2014, doi: 10.1109/LPT.2013.2291571.

[9] C. Cardoux et al., "Room temperature spectral characterization of direct band gap Ge0.85Sn0.15 LEDs and photodiodes," *Proc. SPIE*, 2022, pp. 54–63, doi: 10.1117/12.2608964.

[10] O. Moutanabbir et al., "Monolithic infrared silicon photonics: The rise of (Si)GeSn semiconductors," *Appl. Phys. Lett.*, vol. 118, no. 11, Mar. 2021, Art. no. 110502, doi: 10.1063/5.0043511.

[11] Y. Dong et al., "Germanium-tin on Si avalanche photodiode: Device design and technology demonstration," *IEEE Trans. Electron Devices*, vol. 62, no. 1, pp. 128–135, Jan. 2015, doi: 10.1109/TED.2014.2366205.

[12] Y. Dong et al., "Germanium-tin multiple quantum well on silicon avalanche photodiode for photodetection at two micron wavelength," *Semicond. Sci. Technol.*, vol. 31, no. 9, 2016, Art. no. 095001, doi: 10.1088/0268-1242/31/9/095001.

[13] Y. Miao et al., "Review of Ge(GeSn) and InGaAs avalanche diodes operating in the SWIR spectral region," *Nanomaterials*, vol. 13, no. 3, Jan. 2023, Art. no. 3, doi: 10.3390/nano13030606.

[14] D. Rainko et al., "Investigation of carrier confinement in direct bandgap GeSn/SiGeSn 2D and 0D heterostructures," *Sci. Rep.*, vol. 8, no. 1, Oct. 2018, Art. no. 15557, doi: 10.1038/s41598-018-33820-1.

[15] H. Tran et al., "Systematic study of Ge1−xSnx absorption coefficient and refractive index for the device applications of Si-based optoelectronics," *J. Appl. Phys.*, vol. 119, no. 10, Mar. 2016, Art. no. 103106, doi: 10.1063/1.4943652.

[16] V. R. D'Costa et al., "Sn-alloying as a means of increasing the optical absorption of Ge at the C- and L-telecommunication bands," *Semicond. Sci. Technol.*, vol. 24, no. 11, Oct. 2009, Art. no. 115006, doi: 10.1088/0268-1242/24/11/115006.

[17] T. N. Nunley et al., "Optical constants of germanium and thermally grown germanium dioxide from 0.5 to 6.6eV via a multisample ellipsometry investigation," *J. Vac. Sci. Technol. B*, vol. 34, no. 6, Sep. 2016, Art. no. 061205, doi: 10.1116/1.4963075.

[18] B. Julsgaard et al., "Carrier lifetime of GeSn measured by spectrally resolved picosecond photoluminescence spectroscopy," *Photon. Res.*, vol. 8, no. 6, pp. 788–798, Jun. 2020, doi: 10.1364/PRJ.385096.

[19] P. Ščajev et al., "Temperature dependent carrier lifetime, diffusion coefficient, and diffusion length in $Ge_{0.95}Sn_{0.05}$ epilayer," *J. Appl. Phys.*, vol. 128, no. 11, Sep. 2020, Art. no. 115103, doi: 10.1063/5.0019861.

[20] G. K. Wertheim and G. L. Pearson, "Recombination in plastically deformed Germanium," *Phys. Rev.*, vol. 107, no. 3, pp. 694–698, Aug. 1957, doi: 10.1103/PhysRev.107.694.

[21] G. Wang et al., "A model of threading dislocation density in strain-relaxed Ge and GaAs epitaxial films on Si (100)," *Appl. Phys. Lett.*, vol. 94, no. 10, Mar. 2009, Art. no. 102115, doi: 10.1063/1.3097245.

[22] V. Reboud et al., "Lasing in group-IV materials," in *Silicon Photonics IV: Innovative Frontiers*, D. J. Lockwood and L. Pavesi, Eds. Cham, Switzerland: Springer, 2021, pp. 105–195, doi: 10.1007/978-3-030-68222-4_3.

[23] F. Capasso, "Chapter 1 physics of avalanche photodiodes," in *Lightwave Communications Technology* (Semiconductors and Semimetals), vol. 22, W.T. Tsang, Ed. Amsterdam, The Netherlands: Elsevier, 1985, pp. 1–172, doi: 10.1016/S0080-8784(08)62952-X.

[24] R. J. McIntyre, "Multiplication noise in uniform avalanche diodes," *IEEE Trans. Electron Devices*, vol. ED-13, no. 1, pp. 164–168, Jan. 1966, doi: 10.1109/T-ED.1966.15651.

[25] A. Morales-Acevedo and G. Santana, "Surface recombination velocity in silicon substrates determined from light beam induced current measurements," in *Proc. IEEE Conf. Rec. 25th Photovolt. Specialists Conf.*, 1996, pp. 553–556, doi: 10.1109/PVSC.1996.564066.

[26] F. Pezzoli et al., "Disentangling nonradiative recombination processes in Ge micro-crystals on Si substrates," *Appl. Phys. Lett.*, vol. 108, no. 26, Art. no. 262103, Jun. 2016, doi: 10.1063/1.4955020.

[27] C. Coughlan et al., "Effect of passivation on selectively grown sub-μm Ge-on-Si single photon avalanche diode detectors," in *2023 IEEE Silicon Photon. Conf.*, 2023, pp. 1–2, doi: 10.1109/SiPhotonics55903.2023.10141911.

[28] T. Mikawa et al., "A low-noise n+np germanium avalanche photodiode," *IEEE J. Quantum Electron.*, vol. 17, no. 2, pp. 210–216, Feb. 1981, doi: 10.1109/JQE.1981.1071082.

[29] Y. Okuto and C. R. Crowell, "Threshold energy effect on avalanche breakdown voltage in semiconductor junctions," *Solid-State Electron.*, vol. 18, no. 2, pp. 161–168, Feb. 1975, doi: 10.1016/0038-1101(75)90099-4.

[30] S. Uenoyama and R. Ota, "Monolithic integration of metalens in silicon photomultiplier for improved photodetection efficiency," *Adv. Opt. Mater.*, vol. 10, no. 9, 2022, Art. no. 2102707, doi: 10.1002/adom.202102707.

[31] F. Li et al., "HgCdTe mid-infrared photo response enhanced by monolithically integrated meta-lenses," *Sci Rep.*, vol. 10, no. 1, Apr. 2020, Art. no. 6372, doi: 10.1038/s41598-020-62433-w.

[32] D. Sang et al., "Toward high-efficiency ultrahigh numerical aperture freeform metalens: From vector diffraction theory to topology optimization," *Laser Photon. Rev.*, vol. 16, no. 10, 2022, Art. no. 2200265, doi: 10.1002/lpor.202200265.

[33] M. K. Chen et al., "Principles, functions, and applications of optical Meta-Lens," *Adv. Opt. Mater.*, vol. 9, no. 4, 2021, Art. no. 2001414, doi: 10.1002/adom.202001414.

Lorenzo Finazzi was born in Seriate, Italy, in 1998. He received the bachelor's and master's (*summa cum laude*) degrees in physics engineering in 2020 and 2022, respectively, from Politecnico di Milano, Milan, Italy, where he has been working toward the Ph.D. degree in information technology since 2022. His research interests mainly include the design, development, and characterization of near-infrared germanium and InGaAs/InP single-photon avalanche diodes (SPADs) and mid-infrared GeSn avalanche photodiodes (APDs).

Raffaele Giani was born in Busto Arsizio, Italy, in 1995. He received the bachelor's and master's degrees in physics engineering in 2018 and 2021, respectively, from Politecnico di Milano, Milan, Italy, where he has been working toward the Ph.D. degree in physics since 2021. His research interests include the epitaxy and development and characterization of infrared photodetectors based on group IV materials.

Omar Concepción was born in Havana, Cuba, in 1989. He received the master's degree in physics from the University of Havana, Havana, Cuba, and the Ph.D. degree in nanoscience and nanotechnology from Cinvestav-IPN, Mexico City, Mexico, in 2015 and 2018, respectively. From 2018 to 2021, he was a Postdoc with the University of Twente, Enschede, The Netherlands, working in the epitaxy of topological insulator materials. He is currently a Scientific Researcher of PGI-9, FZJ, with the Group of Silicon-based Epitaxy and Photonics. His research interests include the epitaxial growth of all-Group-IV materials by industry-compatible CVD for photonics, nanoelectronic, energy harvesting, and spintronics applications.

Dan Buca received the master's degree in physics from the Faculty of Physics, University of Bucharest, Bucharest, Romania, in 1999, and the Ph.D. degree in physics (with a dissertation on the SiGe photodetectors) from the University of Cologne, Cologne, Germany, in 2002. He is also a Senior Scientist and Leader of the "Si-based Epitaxy and Photonics" Group with the Peter Gruenberg Institute 9 – Semiconductor Materials, Research Center Juelich (Forschungszentrum Juelich), Jülich, Germany. His research interests include epitaxial growth of group IV materials and their applications in photonics, nanoelectronics, quantum transport, and energy harvesting.

Vincent Reboud received the Ph.D. degree in physics from the University of Paris-Sud, Orsay, France, in 2004. He joined the Tyndall National Institute, Cork, Ireland, and the Catalan Institute of Nanotechnology, Barcelona, Spain, to study three dimensional and reconfigurable optical surfaces. He worked on optoelectronic components patterned by wafer-scale nanoimprint lithography with CEA-LETI, France. In 2014, he joined the Silicon Photonics and then the Optical Sensing Lab of CEA-LETI, as a Senior Scientist. His research interests include IR & MIR photonics platform for a broad range of applications, especially lately on group-IV light sources, and detectors for optical gas sensors.

Giovanni Isella received the Ph.D. degree in physics from the Politecnico di Milano (Polimi), Milan, Italy, in 2001. he was a Postdoc with Solid State Physics Department, ETH Zürich, Zürich, Switzerland. He came back to Physics Department, Polimi, where he is currently Full Professor and a Leader with SiGe Epitaxy Research Group. His research interests include epitaxial growth and characterization of silicon-germanium heterostructures for various applications including: infrared detection, passive and active devices for integrated optics in the near and mid infrared, spintronics, and spin-based semiconductor qubits.

Alberto Tosi (Member, IEEE) was born in Borgomanero, Italy, in 1975. He received the master's degree in electronics engineering and the Ph.D. degree in information technology engineering from the Politecnico di Milano, Milan, Italy, in 2001 and 2005, respectively. From 2006 to 2014, he was an Assistant Professor. Since 2014, he has been an Associate Professor of electronics with the Politecnico di Milano. In 2004, he was a Student with IBM T. J. Watson Research Center, Yorktown Heights, NY, working on optical testing of CMOS circuits. He. His research interests include arrays of silicon SPADs for 2-D and 3-D applications and time-correlated single-photon counting electronics and is currently focusing on silicon and InGaAs/InP single-photon avalanche diodes (SPADs).

Open Access funding provided by 'Politecnico di Milano' within the CRUI CARE Agreement